

Xiu LIU, Zhuo LI, Zexiao WANG, Hyeong Seok YUN, Sheng SHEN

# Design and analysis of electrothermal metasurfaces

© Higher Education Press 2022

**Abstract** Electrothermal metasurfaces have garnered considerable attention owing to their ability to dynamically control thermal infrared radiation. Although previous studies were mainly focused on metasurfaces with infinite unit cells, in practice, the finite-size effect can be a critical design factor for developing thermal metasurfaces with fast response and broad temperature uniformity. Here, we study the thermal metasurfaces consisting of gold nanorods with a finite array size, which can achieve a resonance close to that of the infinite case with only several periods. More importantly, such a small footprint due to the finite array size yields response time down to a nanosecond level. Furthermore, the number of the unit cells in the direction perpendicular to the axis of nanorods is found to be insensitive to the resonance and response time; thus, providing a tunable aspect ratio that can boost the temperature uniformity in the sub-Kelvin level.

**Keywords** modulated thermal infrared radiation, metasurface, nanosecond response time, sub-Kelvin temperature uniformity, finite size, aspect ratio

## 1 Introduction

Metasurfaces, comprising an array of subwavelength scatters, such as metallic nanorods [1–3], graphene nanoribbons [4,5], and dielectric gratings [6], have emerged as a promising platform to actively control thermal infrared radiation [7–12]. The coupling among these thermal scatters or infrared antennas provides multiple degrees of freedom for controlling thermal emission, including its spectrum, directionality, and polarization. The resulting metasurface thermal emitters have become excellent alternatives to semiconductor-

based infrared light sources (e.g., infrared lasers or LEDs) in the lighting [13–15], sensing [16], imaging [17], and energy harvesting [18,19] applications because of their high tunability and low-cost.

However, there still exist substantial challenges for dynamically controlling the thermal infrared emission using active thermal metasurfaces, such as slow temporal response [13,20–22], poor temperature uniformity [23–25], and low emission power. Previous designs for thermal metasurfaces have been mainly focused on the infinite array of subwavelength scatters, which is beneficial for experimental procedures with excellent optical properties [1,3,6] but leads to a slow response speed and non-uniform temperature distribution.

In this study, we investigate the effect of electrothermal metasurface size by designing gold nanorod array (GNA) based metasurfaces with a nearly perfect narrowband emission, shown in Fig. 1(a). The resonance intensity from the finite GNA can be significantly converged to a value comparable to that occurring in the infinite case. The resulting small footprint allows the metasurface thermal emitters to respond at a nanosecond timescale. More importantly, this strong resonance is, to some extent, insensitive to the aspect ratio of the nanorod array, which serves as a new degree of freedom to achieve a temperature uniformity of less than 1 K. Therefore, the comprehensive analysis presented in this study provides a guideline for designing high-performance thermal infrared metasurfaces. A detailed benchmark discussion presented in the Appendix shows that even state-of-the-art active thermal metasurfaces can benefit from our finite-size and aspect-ratio analyses.

## 2 Modeling methods

The optical response of the metasurface was modeled using ANSYS Lumerical finite-difference time-domain solutions. Then, electrothermal simulations were conducted in COMSOL Multiphysics. The GNA was positioned on the multilayer consisting of a Si substrate, 300 nm thick layer of SiO<sub>2</sub> insulation layer, 200 nm thick

Received Apr. 2, 2022; accepted Jul. 19, 2022; online Oct. 20, 2022

Xiu LIU, Zhuo LI, Zexiao WANG, Hyeong Seok YUN, Sheng SHEN (✉)  
Department of Mechanical Engineering, Carnegie Mellon University,  
Pittsburgh, PA 15213, USA  
E-mail: sshen1@cmu.edu

Al reflector, and 100 nm thick dielectric spacer made of  $\text{Al}_2\text{O}_3$ , as shown in Fig. 1(b). The Al reflector also functioned as a heater, where a current is passed through to heat the GNA.

In the optical simulations, the GNA and substrate underneath were illuminated by a plane wave source polarized in the  $x$ -direction, as indicated by the blue arrow in Fig. 1(b). A reflective power monitor was placed above the source to capture the reflective energy and thus the GNA resonance feature.

The thermal simulation combined an electric current module, governed by the electric current equations, with a 3D heat conduction module, governed by heat diffusion equations. In the electric current module, a fixed current of  $I_0 = 250$  mA passed through the Al reflector, and the calculated volumetric Joule heat generation was set to be the heat source in the heat conduction module. The bottom surface of the silicon substrate was fixed to achieve a constant temperature of  $T_0 = 293.15$  K. The transient simulation started with the overall initial temperature of  $T_0$ , and the temperature profiles were captured within 0 to 2000 ns.

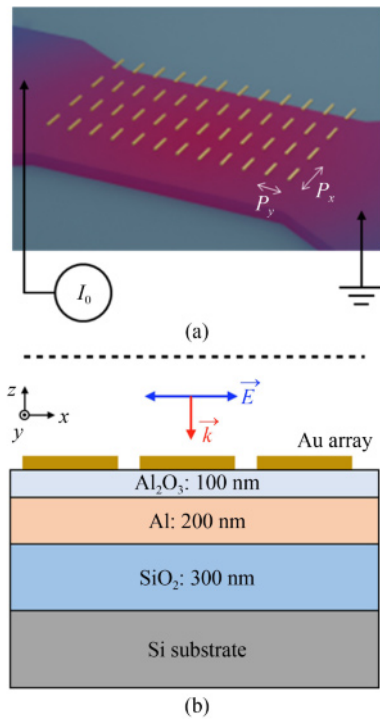


**Fig. 1** Device design and simulation setup.

(a) Schematic of a metasurface based on gold nanorod arrays. (The  $\text{Al}_2\text{O}_3$  spacer is hidden to reveal the Al reflector beneath, which also functions as the heater (Joule heating is applied via a fixed current  $I_0$ ).  $P_x$  and  $P_y$  represent the periodicities in the  $x$ - and  $y$ -directions, respectively.) (b)  $x$ - $z$  view of the simulated device. (The dimensions of each gold nanorod are  $700 \text{ nm} \times 50 \text{ nm} \times 50 \text{ nm}$  in the  $x$ ,  $y$ , and  $z$  directions, respectively. The size and location of the reflective power monitor (dashed line) is fixed throughout simulations.)

## 3 Results and discussion

### 3.1 Optical simulations

To analyze the finite size effect on the metasurface, we first simulated the reflective spectrum of an infinite GNA as a reference. Typically for an infinite GNA, the resonance frequency in the reflective spectra is determined by the localized surface plasmon resonance (LSPR) of the single gold nanorod resonator [26], while the resonance strength is governed by both the LSPR and packing density (periodicity) [27]. Here, we designed the GNA with a single nanorod sized  $700 \text{ nm} \times 50 \text{ nm} \times 50 \text{ nm}$  in the  $x$ -,  $y$ -, and  $z$ -directions, where the periodicities were set to  $P_x = P_y = 800 \text{ nm}$ . The simulated spectrum is plotted as the black line in Fig. 2(a) and features a first-order resonant peak centered around a wavelength of 1046 nm. Figure 2(b) illustrates the  $|E|^2$  profile at the resonance frequency, which indicates a longitude LSPR mode [26]. The high-order mode at around 870 nm in Fig. 2(a) corresponds to the weak periodic brightness near the center of the nanorod depicted in Fig. 2(b).

Subsequently, the effect of the finite array size on the

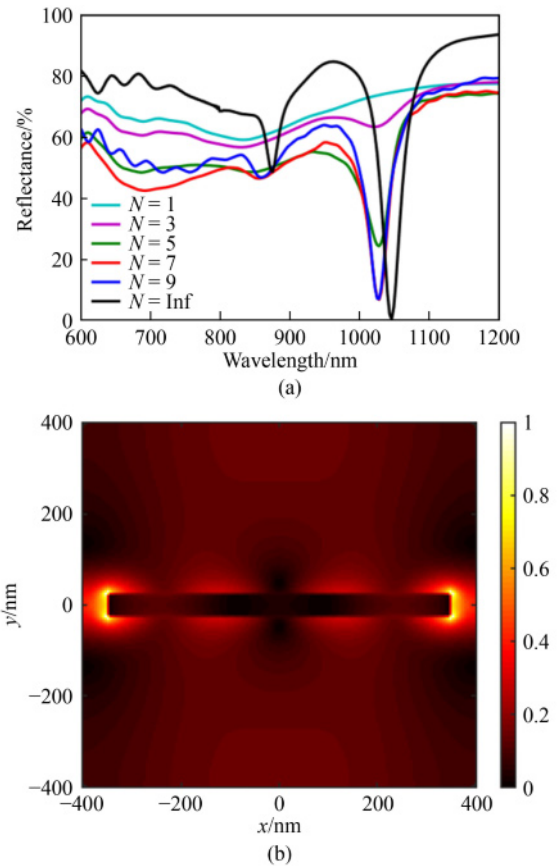


**Fig. 2** Optical simulations for finite-size analysis.

(a) Simulated reflectance spectra for different array sizes; (b) simulated  $|E|^2$  profile of a single unit cell in the infinite array at the resonance wavelength of 1046 nm.

GNA metasurface is investigated with a different finite number of  $N \times N$  arrays from  $N = 1$  to  $N = 9$ , shown in Fig. 2(a). However, for simulations involving finite-size arrays, it is inherently impossible to eliminate the absorption effect of the simulation boundaries (perfectly matched layer) [28], which will inevitably result in an underestimation of the reflectance. Thus, in all finite array size simulations, we fixed the monitor size (fully covered the  $9 \times 9$  arrays) and distance between the monitor and metasurface. By doing so, we could mimic the real experimental condition where the arrays were measured by the same spectrometer. Hence, the reflectance spectra are comparable, and spectral emissivity of those finite-size metasurfaces can be inferred based on Kirchhoff's law.

From Fig. 2(a), we can observe that the finite array preserves the narrowband feature of the infinite one, and the first-order resonance starts to saturate when  $N = 7$ , which corresponds to a metasurface with an approximate area of only  $2.2 \mu\text{m}^2$ . This enabled the device to have a thermal response down to the nanoseconds level, as discussed later in electrothermal simulations. Compared with the case of infinite array size, a red shift in the resonance wavelength could be clearly observed. This shift depends on the packing density or periodicity of the nanorod array, as described by the tight binding model [27]. With an increasing number of nanorods, the dipole moment could be effectively elongated, causing a longer resonance wavelength.

The influence of the GNA arrangement on the reflectance spectra is also studied. To achieve this, we kept the total number of unit cells around 49, which corresponds to a  $7 \times 7$  array marking the resonance saturation, but vary the aspect ratio  $N_x/N_y$  of the array (i.e., number of unit cells along the axial direction ( $x$ -direction) divided by the number along the other ( $y$ -direction)). For arrays with different aspect ratios, the contrast ratio  $C_r$  of the reflectance spectrum was evaluated, which is defined as:

$$C_r = [1 - \min(R)]/[1 - \text{mean}(R)], \quad (1)$$

where  $\min(R)$  represents the minimum value in the reflectance spectrum and  $\text{mean}(R)$  represents the spectral average of the reflectance spectrum. Hence, the contrast ratio physically represents to which degree the resonance feature stands out compared with the spectrum baseline. Therefore, a large  $C_r$  value is targeted.

From Fig. 3(a), for  $N_x/N_y > 1$ , the resonance can maintain its intensity even with only a small number of arrays in the perpendicular direction ( $y$ -axis) owing to the highly polarized nature of the GNA resonance. However, the arrays with an aspect ratio  $N_x/N_y < 1$  exhibit a significantly decreased contrast ratio. A detailed comparison is presented in Fig. 3(b), where  $N_x/N_y = 16/3$  almost keeps the same resonance intensity as that of the unbiased case  $N_x/N_y = 7/7$ , while the peak height of  $N_x/N_y$

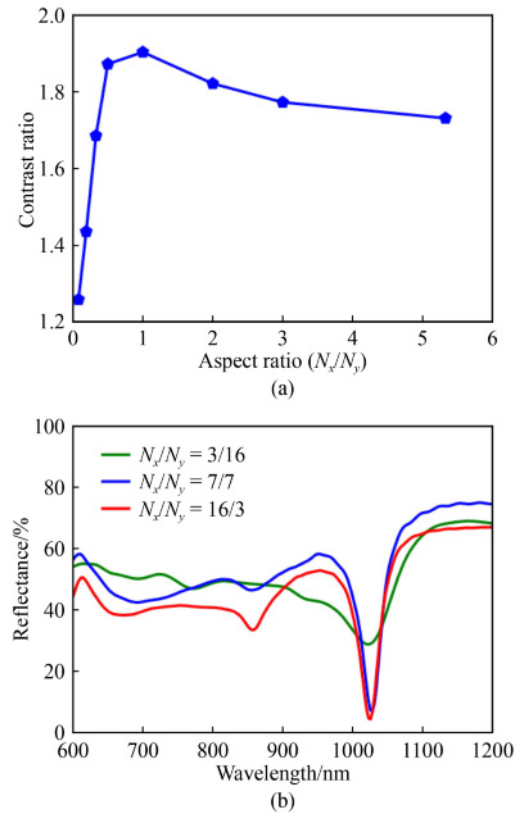


**Fig. 3** Optical simulations for aspect ratio analysis.

(a) Contrast ratios  $C_r$  of finite GNAs with different aspect ratios; (b) simulated reflectance spectra for aspect ratios  $N_x/N_y = 16/3$ ,  $7/7$  and  $3/16$ , respectively.

$= 3/16$  is almost halved and broadened. Relaxing the requirement for the number of arrays in the direction perpendicular to polarization is found to significantly improve the temperature uniformity of the GNA when considering the electrothermal active emission. Thus, it is a valuable factor in design, especially at the nanoscale where the controlling parameters are limited.

### 3.2 Thermal simulations

The GNA is electrically heated, and its emission is analyzed in both transient and steady-states. We first simulate the response time (defined as 90% of the rise time when responding to the on-switch current injection) for the device under different array sizes and aspect ratios. With an increased array size, the response time increases dramatically, shown in Fig. 4, because a larger size induces a larger thermal mass, which significantly reduces the cutoff modulation frequency. This underlines the importance of determining the minimal size of the finite metasurface showing enough resonance contrast. For our device, with a saturation size of  $N = 7$ , we can achieve a response time of approximately 600 ns, which outperforms the majority of current tunable metasurface designs (see Appendix).

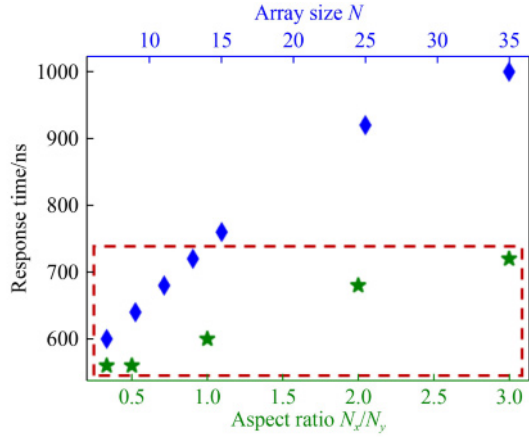


**Fig. 4** Response time for arrays with different sizes  $N$  (blue diamonds) and aspect ratios  $N_x/N_y$  (green stars).

With an array size of approximately  $N = 7$ , containing 49 unit cells, we further study the influence of the aspect ratio. Even under an extremely large aspect ratio change ( $N_x/N_y = 4/12 - 12/4$ ), we can keep the device response time down to nanoseconds, with a fluctuation of only around 100 ns (red-dashed box). Combined with our previous discussion that a large  $N_x/N_y$  has less influence on the resonance contrast of the  $x$ -polarized metasurface, the aspect ratio can provide a stable performance to the metasurface both optically with a narrowband, which indicates nearly perfect emission, and electrothermally with an ultrafast response.

Therefore, under a certain window, the aspect ratio can be set freely to benefit other characteristics of our device performance, among which the temperature uniformity of the metasurface is fundamentally important. A reliable thermal emission typically favors a stable and uniform temperature, which also simplifies the design processes. Even when pursuing advanced nonequilibrium emissions [29], controlling the temperature uniformly in a small local area is a prerequisite for most cases.

The temperature uniformity of the GNA metasurface is illustrated by 2D normalized isothermal contours, shown in Fig. 5(a), along with the geometry of the arrays and electrodes. The GNA with a larger  $N_x/N_y$  is found to have much sparser isothermal contours, indicating a smaller temperature gradient. To specify the details, we also define the temperature difference ( $T_{\max} - T_{\min}$ ) inside the array area enclosed by black-dashed boxes depicted in Fig. 5(a). The temperature difference for both axes in Fig. 5(b) decreases with increasing  $N_x/N_y$ , because of the thermal conduction from the electrode, which substantially modifies the temperature profile of the metasurface. Another indication of the impact from the electrode is that the decrease in temperature difference along the  $y$ -axis is faster than that along the  $x$ -axis due to the more effective heat conduction through the electrode metals. With  $N_x/N_y$  increasing up to about 3, the

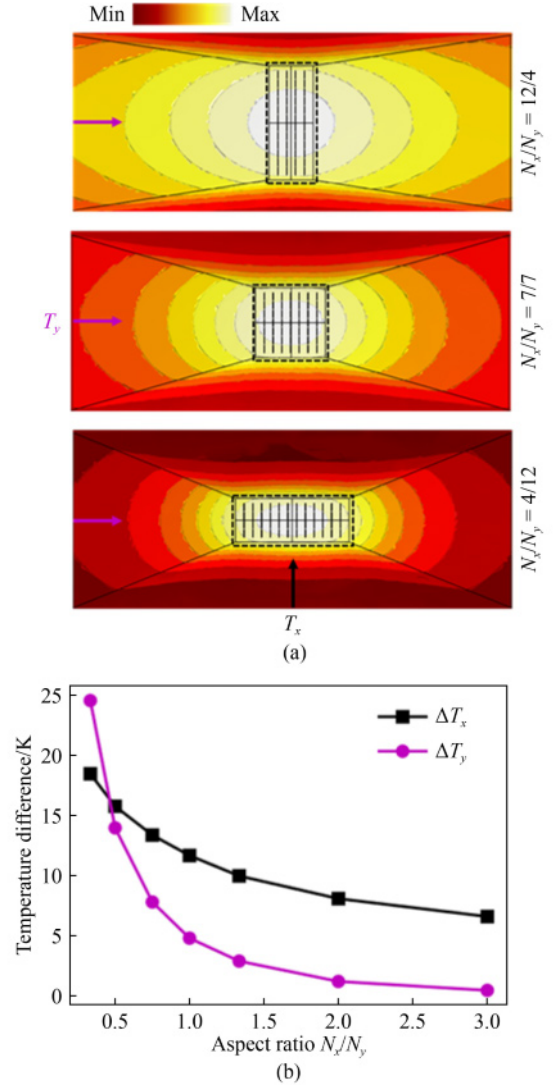


**Fig. 5** Temperature uniformity for arrays with different aspect ratios.

(a) From top to bottom: normalized isothermal contours for arrays with aspect ratios  $N_x/N_y = 12/4$ ,  $7/7$ , and  $4/12$ , respectively; (b) temperature difference along  $x$ -axis  $\Delta T_x$  and along  $y$ -axis  $\Delta T_y$  for arrays with different aspect ratios.

temperature difference can even reach sub-Kelvin levels along the  $y$ -axis while keeping a high resonance contrast ratio of 1.8 and a fast response time of 720 ns. Note that here we only consider a common trapezoidal electrode, whose material and shape can be further optimized based on the GNA aspect ratio to enhance the temperature uniformity. Finally, the degree of freedom in aspect ratio tuning can also improve the power injection into the metasurface via impedance matching based on the maximum power transfer theorem.

## 4 Conclusions

In summary, we designed a thermal metasurface based on

a finite-size gold nanorod array, which can achieve a nearly perfect narrowband emission close to that of the infinite case with only several unit cells. Because of its small volume, the metasurface could achieve a fast response down to a nanosecond level. Moreover, the aspect ratio of this finite array could be tuned to greatly enhance the temperature uniformity to a sub-Kelvin temperature difference, while maintaining the high resonance contrast ratio and nanosecond-level response time. The analysis methodology could be extended to polarization-independent metasurfaces, such as the crossbar array that exhibited better emission efficiency in sensing applications [16,30–33]. Furthermore, our analysis could also be extended to handle inhomogeneous temperature cases based on the framework of a local Kirchhoff's law [34]. While our current conclusions are drawn only considering the normal direction, more physical characteristics can be revealed if the angle dependence of the metasurfaces is included [35,36]. With these extensions, the analyses regarding the size and aspect ratio of the finite-size metasurfaces pave the way for optimizing the electrothermal infrared devices.

**Acknowledgments** This study was primarily supported by the Defense Threat Reduction Agency (Grant No. HDTRA1-19-1-0028) and partially funded by the National Science Foundation (Grant No. CBET-1931964). X. L., Z. L., and Z. W. contributed equally; X. L. and Z. L. identified the problem; Z. L. and X. L. conducted the optical simulations; Z. W. and X. L. conducted the thermal simulations; X. L. and Z. L. prepared the manuscript with the input from Z. W. and H. S. Y.; S. S. supervised the research. All authors have approved the final version of the manuscript. The authors declare no competing financial interest.

## Appendix

The modulation of thermal radiation by a metasurface can be achieved by two mechanisms, namely, temperature and emissivity modulation, both of which can benefit from our finite-size and aspect-ratio analyses. To the best of our knowledge, we have summarized state-of-the-art active thermal metasurface practices in Table A1.

The emissivity modulation by MEMS [20,37], semiconductor carrier injection [22, 13, 38], and graphene gating [39–42] are pure electrical processes whose response times are limited by the electrical device RC time constant. This also holds for the temperature modulation by hot electrons [43], which corresponds to non-resonant emission when electrons and phonons are in non-equilibrium. Therefore, their response times are generally much shorter than our electrothermal approach. Nevertheless, for the optical part of our conclusions, the fast resonance convergence of finite-size array and resonance insensitivity to aspect-ratio, are applicable to these devices to reduce the response time by further eliminating the electrical parasitic capacitance.

The response time for the emissivity modulation by phase-change materials [23–25] is limited by the set pulse, which needs to be long enough for the GeTe-based materials to fully crystallize. This mechanism is particularly suitable for our guidelines regarding both the optical and thermal parts. The response time can be further decreased; accordingly, the temperature uniformity improves as the array size decreases.

The temperature modulation by heat diffusion [34, 21,

**Table A1** State-of-the-art active thermal metasurface

Year	Mechanism	Medium	Wavelength	Response time	Ref
2013	Emissivity	MEMs	6.2 $\mu\text{m}$	30 kHz (33.3 $\mu\text{s}$ )	[20]
2017	Emissivity	MEMs	8.9 $\mu\text{m}$	100 kHz (9.1 $\mu\text{s}$ )	[37]
2014	Emissivity	GaAs/AlGaAs	9.17 $\mu\text{m}$	600 kHz (1.7 $\mu\text{s}$ )	[13]
2018	Emissivity	InAs	7.3 $\mu\text{m}$	4.8 MHz (208.3 ns)	[22]
2019	Emissivity	GaN/AlGaN	4 $\mu\text{m}$	50 kHz (20.0 $\mu\text{s}$ )	[38]
2013	Emissivity	Graphene	7.8 $\mu\text{m}$	40 MHz (25.0 ns)	[39]
2014	Emissivity	Graphene	6.9 $\mu\text{m}$	20 GHz (0.05 ns)	[40]
2016	Emissivity	Graphene	8 $\mu\text{m}$	2.6 GHz (0.38 ns)	[41]
2018	Emissivity	Graphene	8.5 $\mu\text{m}$	7.2 GHz (0.14 ns)	[42]
2021	Emissivity	GSST	1.43 $\mu\text{m}$	500 ms	[23]
2021	Emissivity	GST-326	755 nm	21 $\mu\text{s}$	[24]
2022	Emissivity	GST-225	1.64 $\mu\text{m}$	200 $\mu\text{s}$	[25]
2019	Temperature	Hot electrons	1.59 $\mu\text{m}$	350 ps	[43]
2015	Temperature	Heat diffusion	4.26 $\mu\text{m}$ , 3.95 $\mu\text{m}$	20 Hz (50 ms)	[21]
2018	Temperature	Heat diffusion	4.2 $\mu\text{m}$ , 7 $\mu\text{m}$	100 kHz (10 $\mu\text{s}$ )	[44,45]
2021	Temperature	Heat diffusion	5.1 $\mu\text{m}$	20 MHz (50 ns)	[34]
2022	Temperature	Heat diffusion	1046 nm	600 ns	This study

44–45] is our ideally targeted case. Our research focuses on the metasurface design to handle the tradeoffs between the optical and thermal performances, such as the tradeoff between the infinite-array requirement in optical responses and high speed in thermal responses. However, the response time is a systematic result not only concerning the metasurface layer but also the whole device including the electrode design for heat generation and substrate for heat dissipation. Thus, it is understandable that Ref. [34], after careful optimization of all these factors, has achieved a response time of 20 ns.

Although the temperature uniformity is not comprehensively measured from the reference mentioned above, it remains fundamentally important because most metasurface-based thermal radiation control implicitly assumes that Kirchhoff's law is valid [13,20–25,37–45]. Otherwise, a generalization of Kirchhoff's law [34] or some inhomogeneous direct emission computations [29] must be included, both of which increase the difficulties in design. The temperature uniformity is particularly critical in the phase-change-based modulation, which requires the heat pulse not only appropriate in the time domain but also active in optically functional areas in the space domain.

---

## References

1. Liu B, Gong W, Yu B, et al. Perfect thermal emission by nanoscale transmission line resonators. *Nano Letters*, 2017, 17(2): 666–672
2. Li J, Li Z, Shen S. Degenerate quasi-normal mode theory for near-field radiation between plasmonic structures. *Optics Express*, 2020, 28(23): 34123–34136
3. Li J, Li Z, Liu X, et al. Active control of thermal emission by graphene-nanowire coupled plasmonic metasurfaces. *Physical Review B*, 2022, 106: 115416
4. Lu F, Liu B, Shen S. Infrared wavefront control based on graphene metasurfaces. *Advanced Optical Materials*, 2014, 2(8): 794–799
5. Li J, Liu B, Shen S. Graphene surface plasmons mediated thermal radiation. *Journal of Optics*, 2018, 20(2): 024011
6. Greffet J J, Carminati R, Joulain K, et al. Coherent emission of light by thermal sources. *Nature*, 2002, 416(6876): 61–64
7. Baranov D G, Xiao Y, Nechepurenko I A, et al. Nanophotonic engineering of far-field thermal emitters. 2018, arXiv: 1806.03372
8. Li W, Fan S. Nanophotonic control of thermal radiation for energy applications. *Optics Express*, 2018, 26(12): 15995
9. Ren Z, Chang Y, Ma Y, et al. Leveraging of MEMS technologies for optical metamaterials applications. *Advanced Optical Materials*, 2020, 8(3): 1900653
10. Li Y, Li W, Han T, et al. Transforming heat transfer with thermal metamaterials and devices. *Nature Reviews. Materials*, 2021, 6(6): 488–507
11. Lin Y, Xu Z. Reconfigurable metamaterials for optoelectronic applications. *International Journal of Optomechatronics*, 2020, 14(1): 78–93
12. Miller D A B, Zhu L, Fan S. Universal modal radiation laws for all thermal emitters. *Proceedings of the National Academy of Sciences of the United States of America*, 2017, 114(17): 4336–4341
13. Inoue T, Zoysa M D, Asano T, et al. Realization of dynamic thermal emission control. *Nature Materials*, 2014, 13(10): 928–931
14. Brar V W, Sherrott M C, Jang M S, et al. Electronic modulation of infrared radiation in graphene plasmonic resonators. *Nature Communications*, 2015, 6(1): 7032
15. Park J H, Han S, Nagpal P, et al. Observation of thermal beaming from tungsten and molybdenum bull's eyes. *ACS Photonics*, 2016, 3(3): 494–500
16. Lochbaum A, Fedoryshyn Y, Dorodnyy A, et al. On-chip narrowband thermal emitter for mid-IR optical gas sensing. *ACS Photonics*, 2017, 4(6): 1371–1380
17. Tittel A, Michel A K U, Schäferling M, et al. A switchable mid-infrared plasmonic perfect absorber with multispectral thermal imaging capability. *Advanced Materials*, 2015, 27(31): 4597–4603
18. Lenert A, Bierman D M, Nam Y, et al. A nanophotonic solar thermophotovoltaic device. *Nature Nanotechnology*, 2014, 9(2): 126–130
19. Bierman D M, Lenert A, Chan W R, et al. Enhanced photovoltaic energy conversion using thermally based spectral shaping. *Nature Energy*, 2016, 1(6): 16068
20. Liu X, Padilla W J. Dynamic manipulation of infrared radiation with MEMS metamaterials. *Advanced Optical Materials*, 2013, 1(8): 559–562
21. Miyazaki H T, Kasaya T, Oosato H, et al. Ultraviolet-nanoimprinted packaged metasurface thermal emitters for infrared CO<sub>2</sub> sensing. *Science and Technology of Advanced Materials*, 2015, 16(3): 035005
22. Park J, Kang J H, Liu X, et al. Dynamic thermal emission control with InAs-based plasmonic metasurfaces. *Science Advances*, 2018, 4(12): eaat3163
23. Zhang Y, Fowler C, Liang J, et al. Electrically reconfigurable non-volatile metasurface using low-loss optical phase-change material. *Nature Nanotechnology*, 2021, 16(6): 661–666
24. Wang Y, Landreman P, Schoen D, et al. Electrical tuning of phase-change antennas and metasurfaces. *Nature Nanotechnology*, 2021, 16(6): 667–672
25. Abdollahramezani S, Hemmatyar O, Taghinejad M, et al. Electrically driven reprogrammable phase-change metasurface reaching 80% efficiency. *Nature Communications*, 2022, 13(1): 1696
26. Li J, Wuenschell J, Li Z, et al. Fiber coupled near-field thermoplasmonic emission from gold nanorods at 1100 K. *Small*, 2021, 17(17): e2007274
27. Li J, Yu B, Shen S. Scale law of far-field thermal radiation from plasmonic metasurfaces. *Physical Review Letters*, 2020, 124(13): 137401
28. Berenger J P. A perfectly matched layer for the absorption of electromagnetic waves. *Journal of Computational Physics*, 1994,

- 114(2): 185–200
29. Li Z, Li J, Liu X, et al. Wiener chaos expansion method for thermal radiation from inhomogeneous structures. *Physical Review. B*, 2021, 104(19): 195426
  30. Grant J, Ma Y, Saha S, et al. Polarization insensitive, broadband terahertz metamaterial absorber. *Optics Letters*, 2011, 36(17): 3476–3478
  31. Hasan D, Pitchappa P, Wang J, et al. Novel CMOS-compatible Mo–AlN–Mo platform for metamaterial-based mid-IR absorber. *ACS Photonics*, 2017, 4(2): 302–315
  32. Lochbaum A, Dorodnyy A, Koch U, et al. Compact mid-infrared gas sensing enabled by an all-metamaterial design. *Nano Letters*, 2020, 20(6): 4169–4176
  33. Li D, Zhou H, Hui X, et al. Multifunctional chemical sensing platform based on dual-resonant infrared plasmonic perfect absorber for on-chip detection of poly(ethyl cyanoacrylate). *Advanced Science (Weinheim, Baden-Wurttemberg, Germany)*, 2021, 8(20): 2101879
  34. Wojszwyk L, Nguyen A, Coutrot A L, et al. An incandescent metasurface for quasimonochromatic polarized mid-wave infrared emission modulated beyond 10 MHz. *Nature Communications*, 2021, 12(1): 1492
  35. Mohammadi Estakhri N, Argyropoulos C, Alù A. Graded metascreens to enable a new degree of nanoscale light management. *Philosophical Transactions—Royal Society. Mathematical, Physical, and Engineering Sciences*, 2015, 373(2049): 20140351
  36. Tsitsas N L, Valagiannopoulos C A. Anomalous reflection of visible light by all-dielectric gradient metasurfaces. *Journal of the Optical Society of America. B, Optical Physics*, 2017, 34(7): D1
  37. Liu X, Padilla W J. Reconfigurable room temperature metamaterial infrared emitter. *Optica*, 2017, 4(4): 430–433
  38. Kang D D, Inoue T, Asano T, et al. Electrical modulation of narrowband GaN/AlGaIn quantum-well photonic crystal thermal emitters in mid-wavelength infrared. *ACS Photonics*, 2019, 6(6): 1565–1571
  39. Yao Y, Kats M A, Genevet P, et al. Broad electrical tuning of graphene-loaded plasmonic antennas. *Nano Letters*, 2013, 13(3): 1257–1264
  40. Yao Y, Shankar R, Kats M A, et al. Electrically tunable metasurface perfect absorbers for ultrathin mid-infrared optical modulators. *Nano Letters*, 2014, 14(11): 6526–6532
  41. Fan K, Suen J, Wu X, et al. Graphene metamaterial modulator for free-space thermal radiation. *Optics Express*, 2016, 24(22): 25189–25201
  42. Zeng B, Huang Z, Singh A, et al. Hybrid graphene metasurfaces for high-speed mid-infrared light modulation and single-pixel imaging. *Light, Science & Applications*, 2018, 7(1): 51
  43. Shiue R J, Gao Y, Tan C, et al. Thermal radiation control from hot graphene electrons coupled to a photonic crystal nanocavity. *Nature Communications*, 2019, 10(1): 109
  44. Mahlmeister N H, Lawton L M, Luxmoore I J, et al. Modulation characteristics of graphene-based thermal emitters. *Applied Physics Express*, 2016, 9(1): 012105
  45. Shi C, Mahlmeister N H, Luxmoore I J, et al. Metamaterial-based graphene thermal emitter. *Nano Research*, 2018, 11(7): 3567–3573